Journal of Materials Processing Tech. 316 (2023) 117953

Contents lists available at ScienceDirect

Journal of Materials Processing Tech.

journal homepage: www.elsevier.com/locate/jmatprotec

From conduction to keyhole transition on copper using blue laser: Bead-on-plate process modeling and analysis of physical phenomena

Erica Liverani *, Alessandro Ascari, Luca Tomesani, Alessandro Fortunato

Department of Industrial Engineering (DIN), Alma Mater Studiorum, University of Bologna, viale Risorgimento 2, Bologna, Italy

ARTICLE INFO

Associate Editor: Fenggui Lu

Keywords:
Laser-material interaction
Blue laser
Pure copper
Numerical model
Keyhole

ABSTRACT

The growth of electric mobility has stimulated a large and expanding interest in achieving new manufacturing techniques that would enable more efficient production with less waste. Due to their high levels of flexibility, efficiency, and monitoring capabilities, laser-based processes are essential technologies in this context. Due to high laser absorption of copper for wavelengths under 450 nm, blue lasers are among the most promising laser sources currently on the market and are generating significant interest from battery manufacturers. From a manufacturing point of view, high absorption leads to the possibility of having conduction welding, with calmer melt pool, instead of keyhole welding, characterized by more turbulent molten pool dynamics and higher porosity. On the other hand, consolidated near-IR lasers only lead the possibility of keyhole welding due to poor copper absorptivity with 1064 nm wavelength. In this paper, the transition from conductive to keyhole regime was investigated and predicted through experimental and numerical analyses. From an experimental point of view, the transition is characterized by rapid change of laser absorption and the consequent variation of the seam geometry. Following experimental results, the surface vapor pressure threshold responsible for the transition to the keyhole regime is calculated in accordance with the process parameters employed. Finally, the comparison between experimental and predicted data confirmed the assumption that the recoil pressure is the main physical parameter determining the transition from conduction to keyhole mode, under certain conditions in terms of threshold fluence and irradiance.

1. Introduction

Laser welding of copper or copper-aluminum in dissimilar configuration have received much attention over recent years, in particular due to the high electrical conductivity of these materials useful in the area of e-mobility.

Within this field, extensively work has been done to optimize conventional joining process such as ultrasonic welding and friction stir welding. Good and reliable quality of Cu/Cu spot welded joint was obtained by Ni et al. (2022) who studied the joint formation mechanism and the major cause of joint failure. Same satisfactory results were presented by Kesharwani et al. (2022) for alluminiun/copper hybrid friction stir welding. Although it is possible to generate weld seams with good properties, these conventional technologies are characterized by low flexibility and repeatability. Within this context, a highly rated alternative for industrial application is autogenous laser welding, as clearly shown by Punzel et al. (2020) who compared different continuous-wave laser source for copper welding.

Despite being widely used in many different applications within the electronic and electrical industry, joining of copper presents several challenges due to the high reflectivity at common high-power industrial laser wavelength. Indeed, the absorption at room temperature of copper for near-infrared laser radiation is only 3–5% (Hügel and Dausinger, 2004). This value increases with copper surface's temperature increasing (Hügel and Dausinger, 2004) and with the phase transition from solid to liquid but at the beginning of the welding process the required power is very high. Furthermore, the high thermal conductivity of copper causes the dissipation of the heat input and as a result a difficult in-depth penetration of the welding. This second feature confirms that a significant heat input or preheating process is required to achieve a sufficiently deep penetration depth. Laser power of near-infrared laser sources has improved their quality significantly over the last decade, and today's high-power 10 kW source can be concentrated on a spot of 100 μm, resulting in high power densities. High-brightness laser sources have improved the ultimate performance of copper welding in terms of penetration depth, but spatter, melt

* Correspondence to: viale Risorgimento 2, Bologna 40136, Italy.
E-mail address: erica.liverani2@unibo.it (E. Liverani).

https://doi.org/10.1016/j.jmatprotec.2023.117953
Received 28 October 2022; Received in revised form 1 March 2023; Accepted 20 March 2023
Available online 21 March 2023

material ejection, and porosities remain a problem. Liebl et al. (2014) evaluated a process window for welding with near-infrared laser source ad overcome some process issues identifying in the gas optimization an aid to the improvement of the quality of the joint. Ning et al. (2016) tried to improve the mechanical properties of laser welded copper joint by double-pass laser welding of copper plates, but the desired results were obtained only by adding a post extrusion process on the joint making the overall process complex.

One of the main reasons of the low quality of the welding of copper with lasers is correlated to the weld pool instability due to the extremely high energy required for initial melting. Rüttimann and Holtz (2011) demonstrated that an improvement could be achieved by using power modulation technology. It was also reported that the power modulated laser welding process of copper also produced a greater weld depth by Heider et al. (2011) and Stritt et al. (2011). Ning et al. (2020) reported similar conclusion in case of hybrid welding (laser-arc) of 4 mm-thick T2 pure copper. They observed that the modulation of laser power can reduce the incidence of weld defects such as spatters and pores, and decrease the transverse shrinkage of the weld seam.

A common and well-studied alternative to power modulation is the addition of the beam oscillation at high frequency to the forward movement of the laser head, known as wobble welding. Using this strategy Franco et al. (2021) obtained welds free of defects with 1.5 mm depth by using a multimode beam power with a circular spatial modulation (beam rotation of 0.6–1 mm diameter at 100 Hz frequency). Haubold and Zäh (2019) presented an algorithm for real time spatter detection and the monitoring system showed significant differences in the spatter number and spatter size for varying process parameters and indicates that beam oscillation is suitable for reducing spatter formation.

A more recent approach proposed for improving the efficiency of near-infrared laser is the core-and-ring power distribution obtained with 2-in-1 fiber laser. By using this method, weld seam appearance and process stability are improved compared to conventional single spot solutions.

Generally, the power in the ring area allows the preheating of the copper sheet with an increasing of the abortion coefficient while the power distributed in the core performed the joint. Rinne et al. (2020) demonstrate that the application of core-and-ring power distribution on dissimilar copper-aluminum or copper-steel joints facilitates the mixing of metals inside the weld and helps to avoid cracks. In all configuration this setup promises improved seam quality, reduced spatter formation and increased welding depths. Promising results for enhanced welding quality was also presented by Maina et al. (2018) who evaluate the effect of the power ratio selection between ring and center beams and highlight a huge spatter reduction in the weld bead and surrounding area of aluminum alloy sheets. Mohammadpour et al. (2020) conducted similar tests on mild-steel sheets with improvements in accordance with the other works.

Another possibility to enhance laser copper welding performance is to evaluate laser source with radiation in the visible wavelength spectrum. With this premise, the initial absorption become a secondary problem because reaches values up to 40% at $\lambda = 515$ nm (green wavelength), and up to 50% at $\lambda = 450$ nm (blue wavelength). As consequence, significantly lower power densities are required for copper local melting and high-quality conduction mode welding can be realized. However, high-power laser source with emitted radiation in visible light, present constructive challenges, so currently maximum available power is 3 kW for green laser and 2 kW for blue laser, and in this second case also BPP is quite large compared with near-infrared fiber lasers.

Finally, for copper alloy welding, a hybrid technique combines near-infrared and visible wavelength lasers. Based on the difference in laser absorption in liquid and solid copper, combining multiple wavelengths is helpful for preventing drastic fluctuations of this coefficient. Hess et al. (2011) performed continuous wave laser welding of copper with combined beams at wavelengths of 1030 nm and of 515 nm. Engler et al. (2011) also studied the laser welding process of copper with brilliant green and infrared lasers. Their results showed that the energy coupling efficiency of an infrared laser substantially increased when a keyhole was formed in the molten pool.

Despite the industrial push of laser source producer for using visible wavelength for copper processing, the high costs of this equipment compared to common industrial system and the lack of knowledge about their actual performance did not allow a diffusion of these lasers.

To the best of the authors' knowledge, no papers have investigated in depth the interactions between laser sources with blue wavelengths and pure copper. As a result, no research has been conducted on the methods of interaction downstream of the melting of the material that allow differentiation between interaction in a fully conductive regime, interaction in a transient regime, and finally the onset of keyholes. This need for additional research, in the authors' opinion, becomes especially important for these laser sources, where the maximum powers that can be supplied is lower than for near-infrared fiber lasers and the spot is an order of magnitude larger, is difficult to define an evident transition condition.

In this regard, the proposed paper focuses on assessing the interaction between a high quality and high-power blue laser source on pure copper in order to identify when the transition between conduction vs keyhole occurs.

The effects of laser process parameters on the volume affected by thermal variations, microstructure, and defect formation were studied in 2.3 mm thick commercial pure copper sheets produced by conventional hot rolling process. Irradiance and fluence were intentionally varied from low values characteristic of the conduction heat transfer regime to the higher values permitted by the laser blue source.

Experiment-based tests were used to define a simplified FE model with the goal of identifying and fast-predicting this regime mode transition by evaluating the geometry of laser-affected volume. As long as the heat transfer mode is conduction, the model can determine a linear relationship between the energy actually absorbed by the material and the laser process variables. When entering the keyhole regime, this correlation ceases to be valid, and the model accurately predicts this transition, which is then demonstrated by calculating the maximum superficial temperature and the corresponding surface vapor pressure.

2. Material and methods

2.1. Experimental

2.1.1. Laser-copper interaction

Pure copper (Cu higher than 99.5%) 2.3 mm thick sheets were used for bead on plate linear laser-material interaction experiments. A CW Laserline (Laserline GmbH, Germany) blue laser source (wavelength of 450 nm) characterized by a maximum output power of 1500 W and a 30 mm*mrad beam product parameter (BPP) was used for experimental tests. The beam was delivered with 600 μm (NA 0.2) fiber and was focused with a focal length of 155 mm that allowed a minimum theoretical spot equal to ≈ 490 μm. Laser power and feed rate were varied, as summarized in Table 1, in order to evaluate the interaction between blue laser and copper sheets using a range of values from very low irradiance and fluence (lower powers and/or higher speeds interact with negligible material volume) to the higher values obtainable with the laser source used. Each test will be defined as P_speed in the text (ex. Interaction performed with 1200 W and 5 mm/s will be defined as 1200_5).

Two traces of length equal to 25 mm for each experiment set up was

Table 1
Laser process parameters used in the experimental-based tests.

Power [W]	Speed [mm/s]	Irradiance [MW/cm^2]	Fluence x10^4 [J/cm^2]
1200	5; 10; 30; 50; 70	0.64	0.45–6.24
1350		0.72	0.50–7.02
1500		0.80	0.56–7.8.

carried out in a 100 mm × 35 mm sheet with a distance between adjacent track of 8 mm to avoid thermal influences. After laser processing the sheets were cut with a longitudinal section, as shown in Fig. 1a, for the interaction area characterization and defects analysis.

2.1.2. Interaction area characterization

Metallographic samples were prepared by hot mounting the samples in resin and polishing the final surface by using SiC paper with grit from 800 to 2500 followed by 1 μm alumina suspension. The specimens were etched with a chemical etchant based on ferric chloride (5 g $FeCl_3$, 10 ml HCl, 50 ml glycerol, 30 ml water) with a swab time of 10 s. The area affected by the laser interaction of all samples, specifically the molten and resolidified area morphology, was examined using optical microscopy (OM, Nikon Optiphot-100), and average porosity was calculated using ImageJ free software. More in-depth microstructural analysis was then performed using a SEM-FEG microscope (Tescan Mira3 with Schottky emitter), and the chemical composition of the samples was confirmed using an EDS probe (Bruker X-Flash 630 M) for micro elemental analysis.

Following microstructural analysis, Vickers microhardness tests were performed using a micro-durometer (HX-1000, Remet) with 0.1 kg load (HV0.1) and a dwell time of 12 s. In-depth indentations were made in the middle of the melted and resolidified area, with a space between each indentation of ≈ 120 μm. Longitudinal indentation were positioned, respect to the melt pool depth (P), at P/3 from the surface and include the bulk, the HAZ (Heat Affected Zone) and the fused area. The distance between each indentation was 200 μm in the bulk and in the HAZ, while ≈ 150 μm close and inside the melted area (Fig. 1b).

2.2. Modelling

The aim of the model, that will be explained in this paragraph, was to assess the interaction of the blue wavelength laser beam with a copper sheet identifying the transition between conduction and keyhole with minimal computational costs. It is well known that the laser-material interaction actually requires the modeling of complex physical phenomena. This complexity is increased when the interaction is connected to a phase change, which requires a CFD analysis of the molten metal's motions and the convective heat flux with the environment. These phenomena are supplemented by those that occur when temperatures are high enough to produce the vapor phase of the metal. However, the objective of this work is to develop a more straightforward model that incorporates the majority of the thermal influences on previously described phenomena within the laser beam's absorption coefficient during interaction and is based on experimental validation.

As mentioned above the proposed process simulation is a thermal model and comprise the evaluation of the temperature distribution due to the laser interaction and the phase changes inside the melt-pool. Calculation of the time-dependent temperature field is first performed, based on the intensity of the incident laser beam and copper properties. At this step, copper thermal properties data including latent heat of fusion, thermal conductivity, heat capacity and density are required.

The numerical solution of all equations for the thermal model was done using the finite element analysis (FEA) program COMSOL.

The incident laser beam was described as a boundary heat source with a top hat power distribution defined in Eq. (1):

$$I(x,y) = \frac{4P}{\pi D^2}\frac{1}{4}\left[Erf\left(\frac{D-2x}{2A\sqrt{2}}\right)+Erf\left(\frac{D+2x}{2A\sqrt{2}}\right)\right] \bullet \left[Erf\left(\frac{D-2y}{2A\sqrt{2}}\right)+Erf\left(\frac{D+2y}{2A\sqrt{2}}\right)\right]\left[\frac{W}{mm^2}\right] \quad (1)$$

Where P, D and a are, respectively, the laser power [W], the spot diameter [mm] and A define the rate of decrease in power density from the maximum value to zero. While laser power was defined following the experimental campaign described in Table 1, D and A were fixed and equal to 490 μm and 50 μm, returning the power density distribution reported in Fig. 2a.

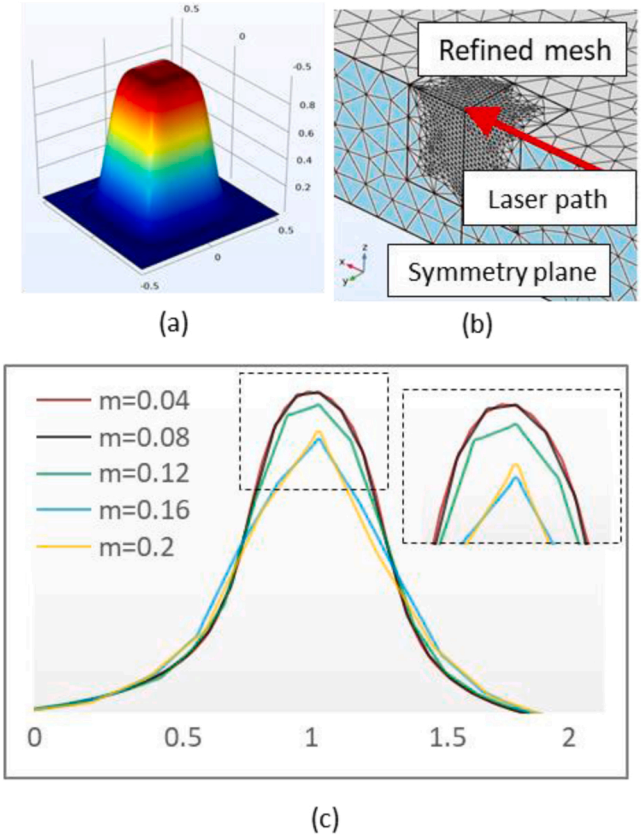

Fig. 2. Power density distribution managed through the ERF function (a), mesh and mesh refinement discretization (b) and mesh dimension optimization inside the probe's volume (c); m parameter defines the maximum element size inside the refinement volume.

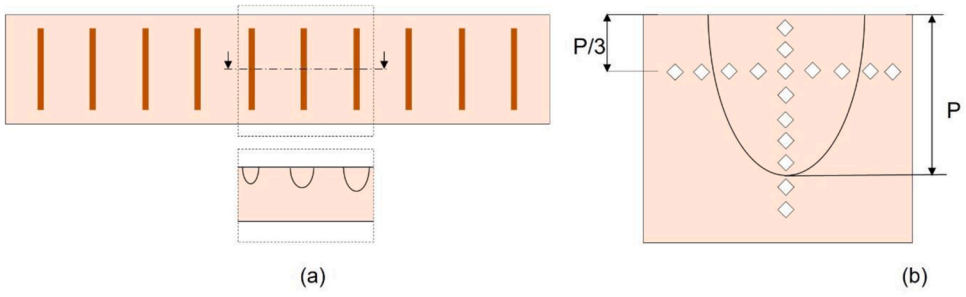

Fig. 1. Laser-material interaction configuration (a) and cross-section of copper plate with hardness measurements' location (b).

The amount of energy delivered to the target was calculated using the target material's absorption coefficient. In particular, in accordance with the literature, copper's absorption with the interaction of the blue wavelength was initially thought to be equal to 0.6 and was later modified to obtain the best prediction of the geometry of the molten and resolidified material in terms of width and depth.

The heat capacity and thermal conductivity of solid copper were determined experimentally up to 300 °C using a comparative method (ASTM E 1461–07) and LFA 447 Nano Flash Netzsch equipment. Based on literature considerations, the same properties were defined after 300 °C, as well as the density and the coefficient of thermal expansion. Table 2 reports in detail all the temperature-dependent properties.

All these physical parameters are then utilized in Fourier's equation (Eq. 2) to resolve the time-dependent temperature distribution in the material during laser interaction.

$$\rho C_p \frac{\partial T}{\partial t} + Q = \nabla(k \nabla T) \tag{2}$$

Where ρ is the copper density [kg/m^3], Cp is the heat capacity at constant pressure [J/(kg· K)], k is the thermal conductivity [W/(m· K)], Q the absorbed energy density [W/m^3], T the temperature [K] and t the time [s]. Radiant heat losses were considered negligible, while convective heat losses in air were considered setting an ambient air temperature of 25 °C.

As concern the mushy zone, where solid and liquid phases coexist, the material properties were redefined by the software on the basis of solidus and liquidus temperature following Eqs. (3)–(5) where θ_s and θ_l are the phase fraction of solid and liquid material respectively, α_m is the mass fraction and $L_{s\rightarrow l}$ is the latent heat absorbed from solid phase to liquid phase (207 kJ/kg).

$$\rho = \theta_s \rho_s + \theta_l \rho_l \tag{3}$$

$$C_p = \frac{1}{\rho}\left(\theta_s \rho_s C_{p,s} + \theta_l \rho_l C_{p,l}\right) + L_{s\rightarrow l}\frac{\partial \alpha_m}{\partial T} \tag{4}$$

$$k = \theta_s k_s + \theta_l k_l \tag{5}$$

Tetrahedral mesh elements are used in the whole domain. Since the physic phenomenon principally involves the area along the laser path, this domain is meshed with finer size elements than the surrounding part. Far from the welding area, elements with maximum dimension of 0.5 mm were set, while a mesh dimension optimization was performed close to the laser path to gain enough confidence in the accuracy of the model while not exceeding the available computational resources. A size-controlled parameter was set inside volumetric block domain with dimension 1×1x 2.3 mm^3 defined in the middle of the laser path Fig. 2b. The parameter "m" defines the maximum element size inside this volume and a parametric sweep study was set changing m from 40 to 200 μm. From this analysis a maximum element size was set equal to 80 μm, since lower values had negligible effect on the final results, in terms of melt pool dimension (<2%), as show in Fig. 2c.

The influence of liquid flow on the temperature field significantly affects the dimension of the phase-change volume thus, in a second time, a refinement of the thermal model was performed by adding the effect of fluid motion inside the weld pool. The Computational Fluid Dynamics (CFD) model was set up by activating the natural convection and Marangoni effect while, the effect of vapor loss on thermal profile was not considered. The viscosity data is further required in CFD model and the input data are reported in Table 2.

3. Results

3.1. Experimental analysis

3.1.1. Geometry

Representative cross sections of the laser processed path obtained with different process parameters (Power, Laser speed, Irradiance and Fluence) are shown in Fig. 3, while mean measurements of depth and width, respectively in column 5 and 6, of the melted area are reported in Table 3. As expected, the interaction area dimension decreases as the laser moving speed increases since the heat input, in terms of linear energy density, decreases as well. Maximum depth (d) of 0.78 mm was measured with laser speed of 5 mm/s and power of 1500 W and the correspondent width (w) was 0.82 mm, with a resulting aspect ratio (d/w) of 0.95.

After a more accurate analysis of the geometric data, it is possible to

Table 2
Copper temperature-dependent thermophysical properties at solid and molten state (Baba et al. (2012), Assaela et al. (2010)). Grey cell contains the results of experimental data performed in this work.

T [K]	Density [kg/m^3]	Viscosity [mPa•s]	Surface tension	Heat Capacity [J/kg•K]	Thermal conductivity [W/m•K]
300	8930	/	/	407.0	330.6
350				409.0	323.6
400				410.0	316.7
450				411.0	310.0
500				412.0	303.5
550				413.0	297.1
600				414.0	290.9
700				416.6	278.8
800				419.0	267.4
900				421.2	256.5
1000				423.5	246.3
1100				425.8	236.7
1200				428.1	227.6
1300				430.4	219.2
1356 (solid)				431.7	214.7
1356 (liquid)	7998	4.03	1313.2	3300.0	157.2
1400	7962	3.74	1305.6	800.0	159.4
1500	7881	3.21	1288		164.4
1600	7799	2.81	1270.4		169.3
1700	7717	2.50	1252.8		174.3
1800	7635	2.25	1235.2		179.3
1900	7553	2.05	1217.6		184.3
1950	7512	1.96	1206		186.7
2000			1200		
3000			1024		
3500			936		

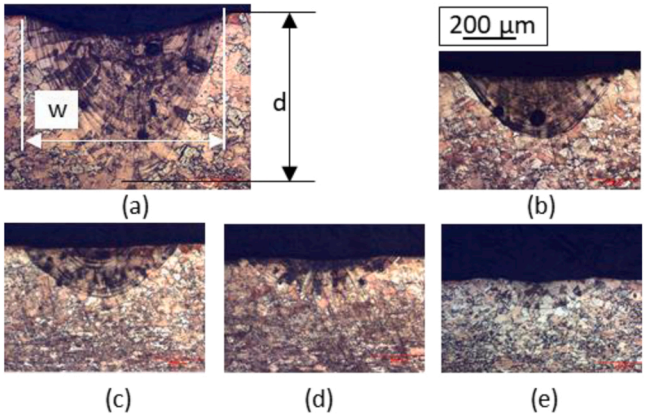

Fig. 3. Geometry of the laser-copper interaction area of 1350_5 (a), 1350_10 (b), 1350_30 (c), 1350_50 (d), 1350_70 (e) samples.

Table 3
Summary of the average measurements of depth and width as the process parameters vary (P = Power, v=laser speed, I=Irradiance, F=Fluence, d=seam depth, w=seam width).

1 P [W]	2 v [mm/s]	3 I [MW/cm^2]	4 F (x10^4) [J/cm^2]	5 d [mm]	6 w [mm]	7 Aspect Ratio (d/w)
1500	5	0.80	7.80	0.78	0.82	0.95
1500	10	0.80	3.90	0.57	0.77	0.74
1500	30	0.80	1.30	0.21	0.61	0.34
1500	50	0.80	0.78	0.16	0.59	0.27
1500	70	0.80	0.56	0.14	0.57	0.25
1350	5	0.72	7.02	0.64	0.79	0.81
1350	10	0.72	3.52	0.33	0.64	0.52
1350	30	0.72	1.17	0.2	0.59	0.34
1350	50	0.72	0.70	0.14	0.56	0.25
1350	70	0.72	0.50	0.13	0.55	0.24
1200	5	0.64	6.24	0.43	0.66	0.65
1200	10	0.64	3.12	0.24	0.6	0.4
1200	30	0.64	1.04	0.15	0.52	0.29
1200	50	0.64	0.62	0.11	0.47	0.23
1200	70	0.64	0.45	0.1	0.45	0.22

highlight some interesting aspects. In Table 4 the degree of association between geometrical and process parameters is measured by a correlation coefficient, denoted by R (or Pearson's correlation coefficient). The correlation coefficient is measured on a scale that varies from + 1 through 0 to − 1. Complete correlation between two variables is expressed by either + 1 (positive correlation) or − 1 (negative correlation), while complete absence of correlation is represented by 0. In Table 4 five classes of correlation were highlighted from very weak (light blue) to very strong (dark blue) correlation. The results show a very strong correlation of the seam geometry, in particular its depth, with laser fluence, while power (or irradiance) have a marginal effect on the final depth (weak) and a moderate impact on the width.

3.1.2. Defects

Defect analysis and in particular porosity percentage inside the melted and resolidified copper was correlated to the fluence. By classifying the fluence values used in three classes as follows: 1–2.5 (x10^4) J/cm^2, 2.6–5 (x10^4) J/cm^2, > 5 (x10^4) J/cm^2 it is evident that the porosity increases when the fluence increases with the following measured mean values: 0.7%, 2.6%, 3.5%. In all cases, the percentages of pores are below 5%, however several large pores have been detected in some sections of the specimens, mainly if higher fluences were defined, in agreement with the average values presented. An example of these macro pores is shown in Fig. 4. These defects can be categorized as "keyhole stability defects" in accordance with the increased porosities with fluence and the identified geometry of these pores, which appears rounded in shape. In fact, the stability of the keyhole and the ultimate weld-bead quality are strictly correlated in deep penetration welding of metals. The keyhole becomes unstable and collapses as the heat input rises (greater fluence), isolating the gas inside and causing bubbles to form and resulting spherical porosities.

Analyzing the micrograph sections of welded beads, it was possible to highlight that the fluence does not only affect the geometry of the bead and the percentage of porosity, but also the position of the pores. In order to evaluate a correlation between laser parameters and porosity distribution, the bead was virtually divided into two parts: a central area (C) with depth and width equal to 80% of the bead size and an interface area (I) as shown in Fig. 5 as an example. For both areas, the relative porosity was calculated and this data was correlated with the fluence values for each sample.

This correlation shows an increasing of porosities in the interface between base-material and melted material at fluence decreasing, while for high fluences most of the pores are concentrated within the bead. This relationship is shown in Fig. 6, and the relative porosity, which is determined by dividing the porosity in the area of interest by the total porosity of the joint, increases with fluence in the central area (it will complementarily decrease in the area at the interface).

3.1.3. Microstructure and hardness

Samples 1500_5 and 1500_50 were used in this section in order to show the weld beads properties in terms of microstructure evolution and hardness. The weld bead grain morphology in the fused zone (FZ), in the heat affected zone (HAZ), and in close proximity to the base material are highlighted in Fig. 7 and Fig. 8 by optical micrographs and SEM magnification. Equiaxed grains at the FZ's core and close to the surface are followed by highly elongated grains oriented in the direction of the heat flow and which extend up to the HAZ. In the HAZ coarser elliptical-shaped grains and abundant annealing twins are visible and their dimension decrease moving away from the joint. The chemical composition of the base material and inside the weld was carried out by EDS analysis and the results (Table in Fig. 7) confirm the purity of the copper sheet.

According to the results of the microstructural analysis, the hardness measurements on the 1500_5 exhibit higher hardness (mean 114 HV0.1,

Table 4
Correlation factor between geometric and process parameters.

	Depth (d)	Width (w)	d/w
Power/Irradiance	0.32	0.51	0.26
Speed	-0.77	-0.76	-0.82
Fluence	0.94	0.87	0.96

Very strong
Strong
Moderate
Weak
Very Weak

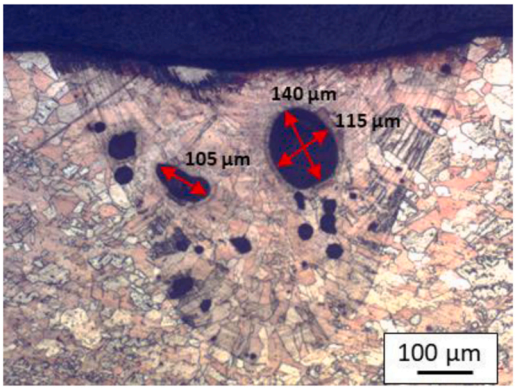

Fig. 4. Representative cross-section (1500_10) for the evaluation of large pores dimension.

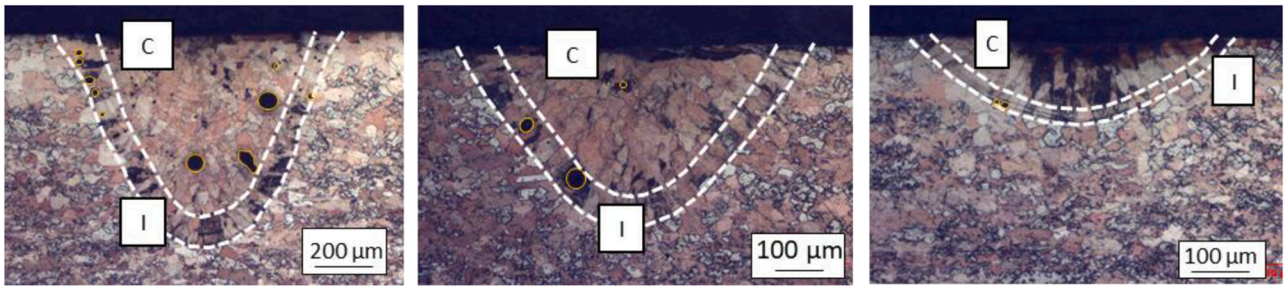

Fig. 5. Internal-external porosity measurement method. From the left the cross section of 1500_5, 1500_30 and 1500_50 samples are shown.

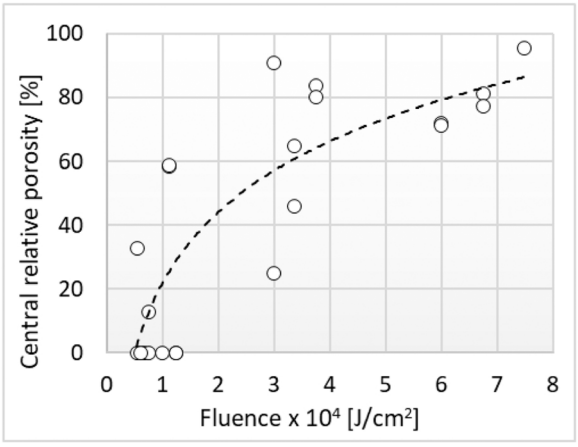

Fig. 6. Correlation between relative porosity in the central (C) and interface (I) areas for different fluence levels.

standard deviation 5.8) in the melt pool, lower values (mean 67 HV0.1, standard deviation 3) in the HAZ, and intermediate values (mean 78 HV0.1, standard deviation 2.8) in the base material. Hardness measurement of 1500_50 sample confirm the same match with microstructural investigation and following values were identified: 98 HV0.1 in the melt pool, 70 HV0.1 in the HAZ and 76 HV0.1 (standard deviation 2.4) in the base material. The standard deviation cannot be calculated in that case due to the small size of the melt pool and HAZ. Fig. 9 displays the longitudinal and transverse profiles of hardness of both samples. The extension of the HAZ may be determined from the hardness profile and, for maximum fluence, reaches widths of 2.7 mm near the surface and 1.3 mm in depth, while for reduced fluence, the corresponding values are 0.5 mm and 0.8 mm.

3.2. Model analysis

As was already mentioned, a parametric simulation was first run, and the absorption coefficient was varied to range from 0.20 to 0.60 for each set of process parameters. Columns 5 and 6 in Table 5 contain the results of the laser-material interaction's area in terms of predicted depth (d_M) and width (w_M), comparable with experimental measurements. The simulation that best predicts the real geometry has been chosen, and the relative absorption coefficient value is reported in column 8. Instead, Column 7 displays the average percentage error calculated on the width and depth of the area of interest, expressed as an absolute value.

Plotting the data of the resulting absorption coefficient and the calculated prediction error with respect to the fluence used for each test

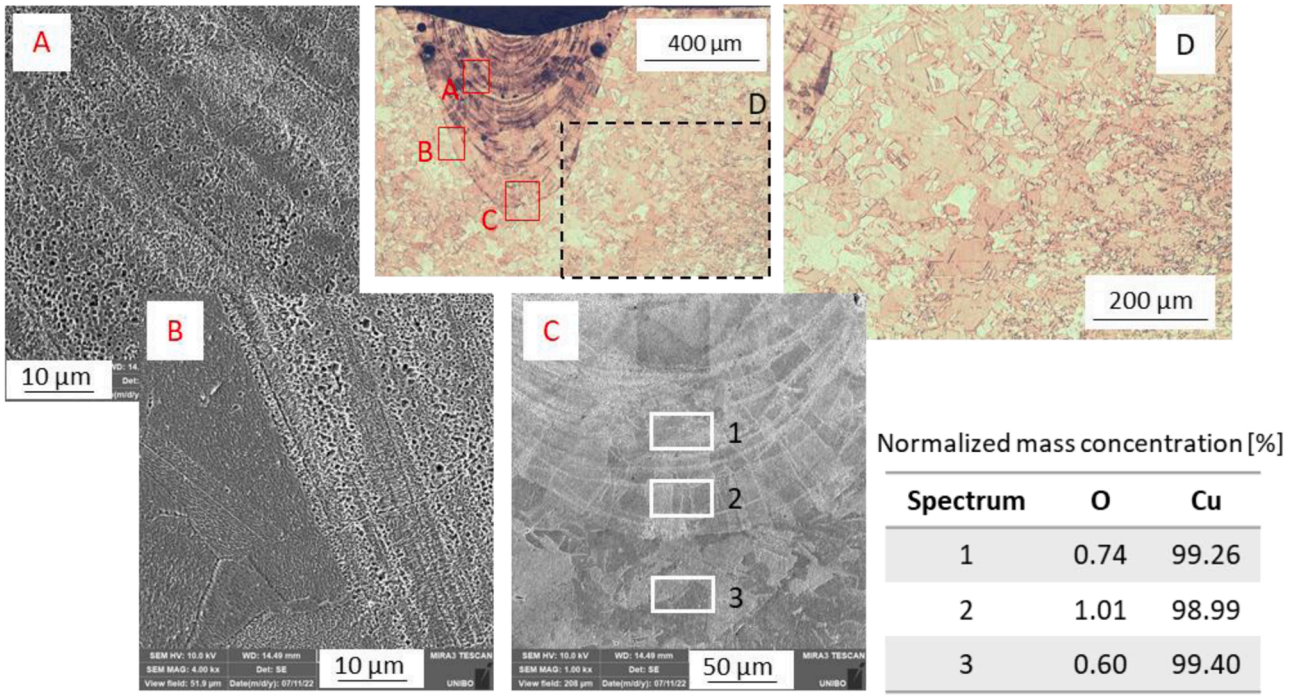

Normalized mass concentration [%]

Spectrum	O	Cu
1	0.74	99.26
2	1.01	98.99
3	0.60	99.40

Fig. 7. 1500_5 microstructure inside the melted and resolidified area (A-B), in the interface edge (C) and in the heat affected area (D) captured by OM and SEM. Microanalysis in three different small area of the samples is also shown in the table.

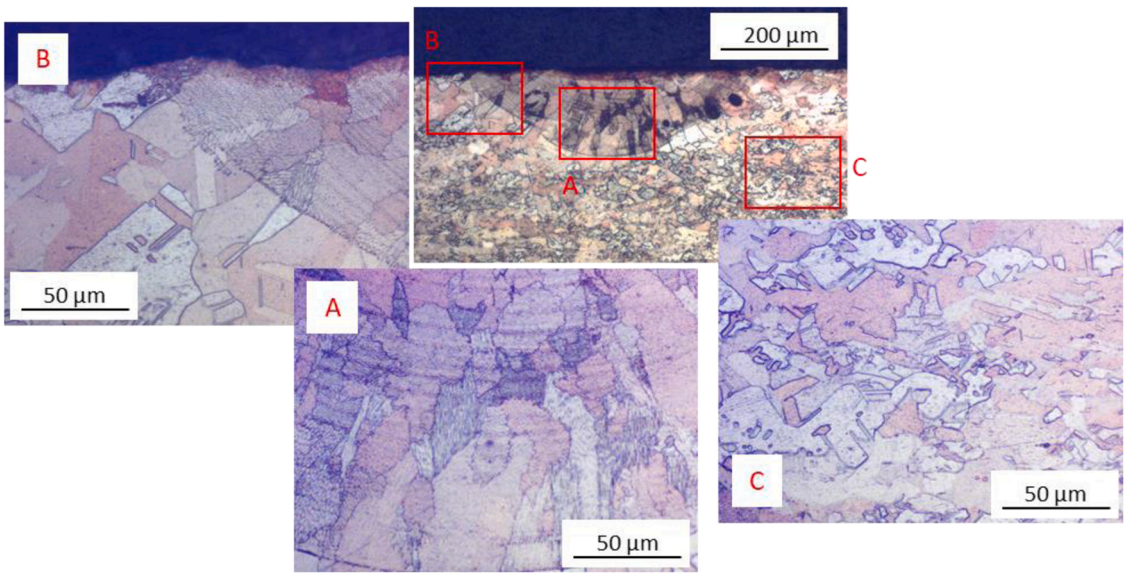

Fig. 8. 1500_50 microstructure inside the melted and resolidified area (A), in the interface edge (A) and in the heat affected area (C).

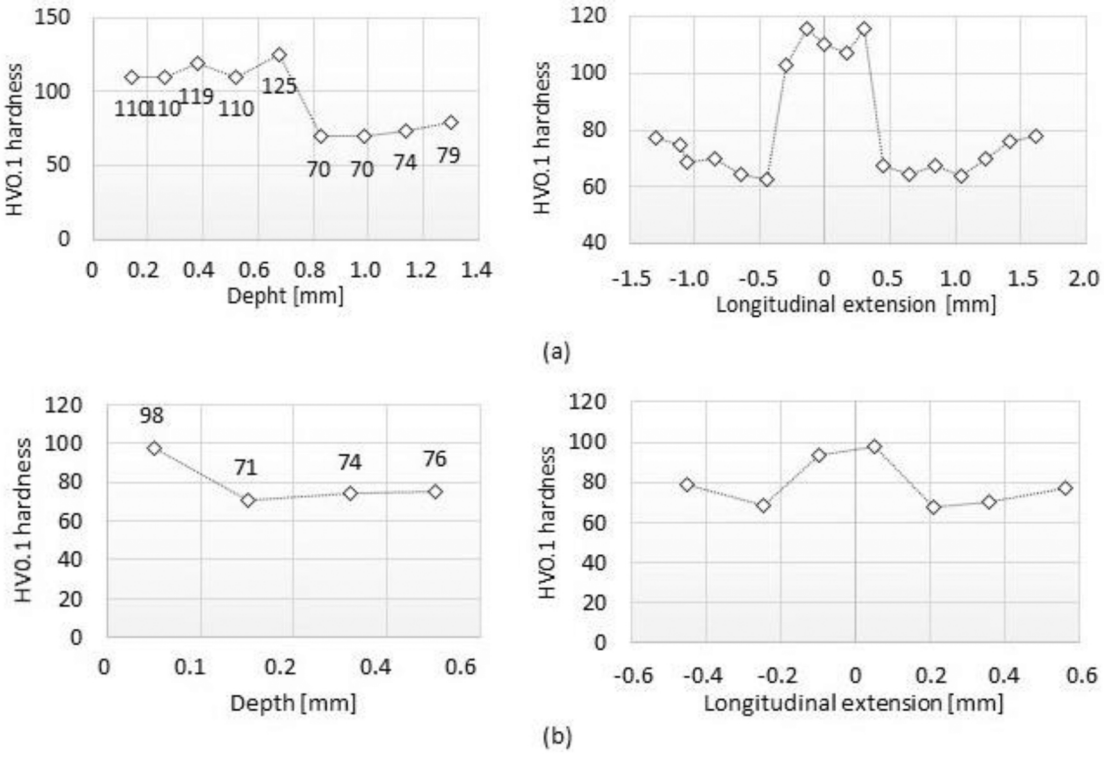

Fig. 9. Longitudinal and transverse hardness profile carried out on 1500_5 (a) and 1500_50 (b) respecting the scheme shown in Fig. 1.

both these factors increase linearly. This relationship is clearly shown on the graph in Fig. 10, and the regression line that was obtained has a very high correlation factor, greater than 0.8 for both variables.

From Fig. 10 analysis is possible to highlighted two different issues: (1) the obtained absorption coefficients (from 0.23 to 0.35) are significantly lower than expected values (around 0.6) and (2) average geometric error predicted by the models significantly increases with fluence up to values greater than 30%.

As previously stated, the prediction error has been provided as the average of the error between width and depth expressed as an absolute value. However, to better understand what causes the increasing of the error, an analysis of the aspect ratio (depth/width) of the real and simulated melted zones is required, and Fig. 11 permits a more intuitive comparison. The figure depicts a simplified geometry of the real (green) and simulated (red) melted zones in the form of a table. All boxes with a difference of more than 15% between these two curves have a gray cross at the bottom left highlighted. In all these cases, the real fused areas are deeper and narrower than the simulated ones, resulting in higher aspect ratios. The differences in the aspect ratio between real measurement and calculated simulation increases with fluence because the predicted melted area is less sensitive to laser process parameters as shown in Fig. 12 based on the comparison between column 7 of Table 3 and

Table 5
Summary of depth and width calculated by FE simulations (columns 5–6), comparison with experimental data (column 7), resulting absorpion coefficient (column 8) and aspect ratio (column 9).

1 Test	3 I [MW/cm^2]	4 F x10^4 [J/cm^2]	5 d_M [mm]	6 w_M [mm]	7 |e| [%]	8 Ca	9 Aspect Ratio $(d/w)_M$
1500_5	0.80	7.80	0.49	1.09	35.4	0.33	0.45
1500_10	0.80	3.90	0.42	0.98	26.8	0.35	0.43
1500_30	0.80	1.30	0.20	0.62	3.5	0.25	0.32
1500_50	0.80	0.78	0.16	0.59	0.3	0.24	0.27
1500_70	0.80	0.56	0.14	0.55	2.5	0.23	0.25
1350_5	0.72	7.02	0.45	1.04	30.2	0.35	0.44
1350_10	0.72	3.51	0.28	0.75	15.9	0.3	0.38
1350_30	0.72	1.17	0.19	0.61	4.8	0.27	0.31
1350_50	0.72	0.70	0.13	0.54	3.9	0.24	0.25
1350_70	0.72	0.50	0.12	0.52	5.8	0.24	0.23
1200_5	0.64	6.24	0.31	0.81	24.9	0.32	0.39
1200_10	0.64	3.12	0.22	0.66	10.0	0.29	0.33
1200_30	0.64	1.04	0.14	0.55	6.4	0.26	0.24
1200_50	0.64	0.62	0.11	0.50	3.9	0.25	0.22
1200_70	0.64	0.45	0.10	0.48	3.4	0.25	0.21

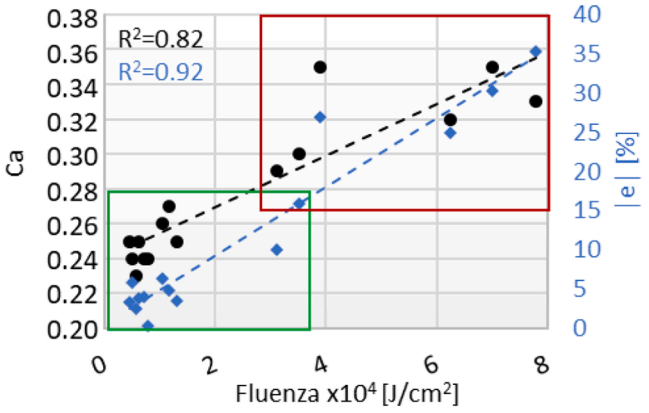

Fig. 10. Absorption coefficient resulting from the comparison between real and simulated data at the variation of fluence and relative average error.

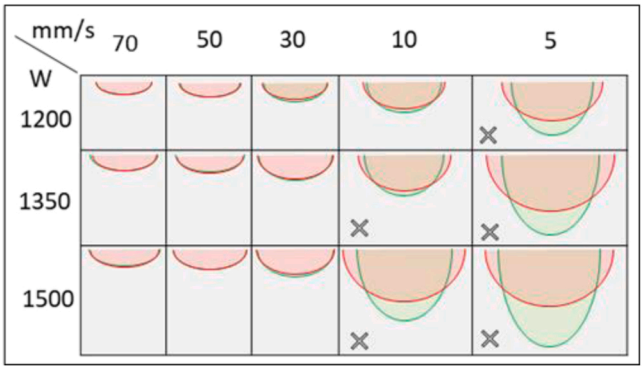

Fig. 11. Melt pool geometry at different laser power and laser speed: measured (green) and simulated (red) dimensions.

column 9 of Table 5.

A further analysis of the resulting data was necessary to ensure that the discrepancy between model and reality was not due to an over-simplification of the model. The effect of CFD physics on absorption coefficient calibration and melted area aspect ratio was evaluated and for comparison the 1350_5 model was used. Non-isothermal and heat transfer modulus have been combined to simulate fluid flows with

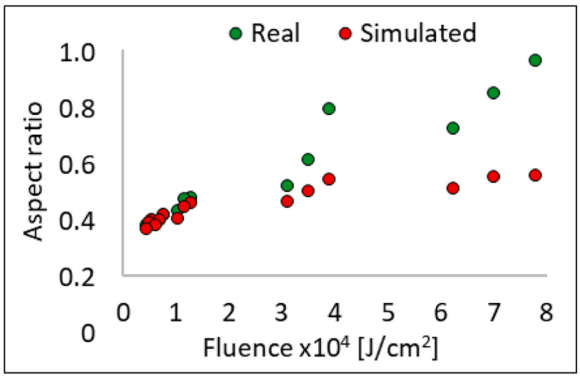

Fig. 12. Aspect ratio (depth/width) of the melt pool geometry: measured (green) and simulated (red).

temperature-dependent fluid properties. Fig. 13a depicts this effect, with a significant decrease in width (−26%) and depth (−21.8%) of the melted area clearly visible. The maximum temperature falls from 3680 °C to 2662 °C. To restore the actual geometry prediction, the absorption coefficient was increased from 0.35 to 0.46 (+31%) and the temperature field in a mid-section of the samples is shown in Fig. 13b.

The definition of a more complex model that takes into account the dynamics of the melt pool and, in particular, the Marangoni effect and buoyancy forces, has a significant influence on the dimension of the melt pool if the model is not further calibrated, but not on the aspect ratio. The calculated aspect ratio continues to be 0.44 as in the thermal model and far from the measured aspect ratio (0.81).

4. Discussion

The results of the proposed model, when compared to those obtained experimentally, show that the model can correctly predict (error < 10%) the size of the volume of molten and resolidified material only for lower fluence values; specifically, fluences less than 3.5×10^4 J/cm^2. This discrepancy was not resolved by including a temperature-dependent laminar flow effect in the model. In fact, the introduction of CFD physics enabled to identify absorption coefficient values that were closest to those expected (which being between 0.6 and 0.7), but it did not provide a solution to the average error on the size. In the case 1350_5, used as an example, the aspect ratio of the melted zone is equal to 0.46, with a minimum variation compared to the model without laminar flow (0.44) and thus far from the true value of 0.81. The solution to this discrepancy between model and real interaction must thus be found in the different mode of interaction, which moves from conduction to keyhole. This is demonstrated analytically by determining whether the energetic conditions are actually attributable to an initial phase of keyhole triggering. The following threshold parameters can be determined from the literature and are required for the transition to keyhole:

- Irradiance: Cunningham et al. (2019) stated that a material-dependent critical irradiance on the order of 0.5 MW/cm^2 can be defined, over which the keyhole mode is active.
- Aspect ratio: Cunningham et al. (2019) and Nakamura et al. (2000) stated that keyhole mode interaction occurs when the aspect ratio is higher than 0.5.
- Exceeding of the boiling temperature for enabling the vapor surface pressure to cause a keyhole formation as mentioned by Wu et al. (2023): in case of pure copper the boiling temperature is 2562 °C.

According to Table 3, all the tests were performed with irradiance values greater than 0.5 MW/cm^2, implying that the energy density supplied to the laser-material system is sufficient to generate the keyhole

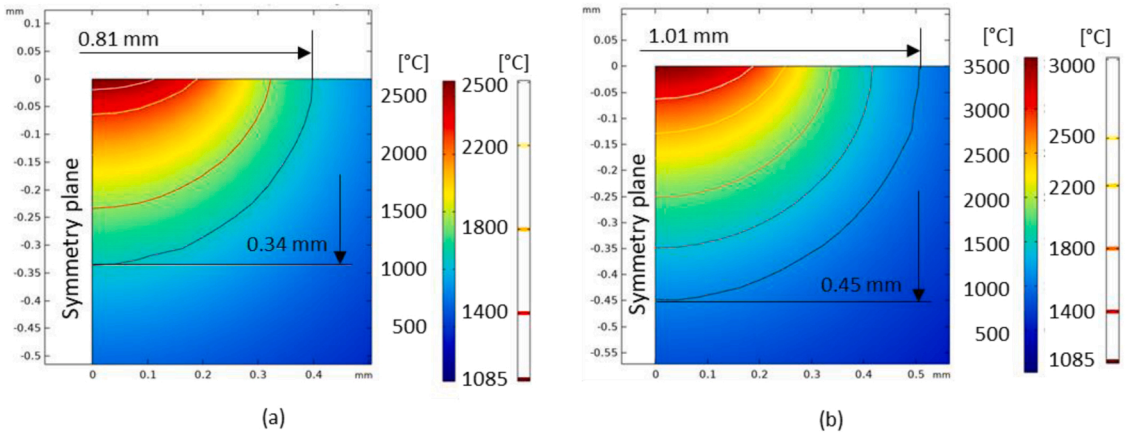

Fig. 13. CFD main effects impact on melted area geometry and aspect ratio before (a) and after (b) absorption coefficient re-calibration.

in all conditions tested. In contrast, aspect ratios value greater than 0.5 were only measured in some samples, and these correspond exactly to the tests for which there is a divergence between model and experiments. For these tests the maximum superficial temperature and the temperature heating rate, after melting, were calculated and resulting values are reported in Table 6.

As stated, confirms that all the necessary requirements were verified in 1500_5, 1500_10,1350_5,1350_10 and 1200_5 process conditions.

In order to univocally settles the conduction-to-keyhole transition, the vapor surface pression must be assessed. In fact, following Cunningham et al. (2019), once the surface temperature reaches the boiling point, localized and superficial vaporization formed a depression, which will in turn originate in the keyhole. The surface pressure can be calculated with Clasius-Clapeyron equation (Eq. 6):

$$p_s = p_0 e^{\Delta Hm/k_B(1/T_b - 1/T_s)} \tag{6}$$

Where p_0 is the working ambient pressure and the pressure at which the boiling point is defined (1 atm); ΔH is the heat of vaporization per atom (5.069×10^6 [J/kg]); m is the copper atomic mass ($1{,}0552061 \times 10^{-25}$ [kg]); k_B is the Boltzmann's constant ($1{,}380649 \times 10^{-23}$ [J/K]); T_B is the boiling temperature (2835 [K]) and T_s is the surface temperature.

Clasius-Clapeyron allows calculating the surface pressure with the assumption of constancy of the material volume due to the high heating rate ($>10^4$ K/s); heating rates in the order of magnitude of those actually calculated for the conditions under study (Table 6).

From the models' results it is possible to calculate the vapor surface pressure (p_s) considering the maximum reached temperature as shown in Fig. 14.

The pressure must be greater than the ambient pressure for the vapor depression to penetrate the melt pool and causes a significant displacement of liquid from the laser-material interaction region. Based on the results, the 1200_5 and 1350_10 tests represent a near-transition condition, whereas the pressure of 22.8 bar reached by the 1350_5 parameters can be considered the first case of this study in which a keyhole regime is completely reached. Consequently, also fluences' threshold for conduction-to-keyhole transition and keyhole obtainment can be calculated and their values are respectively 3.52×10^4 J/cm^2 and 7.02×10^4 J/cm^2.

The results obtained from the model's data analysis also allow for some additional observations on the microstructure analysis and the

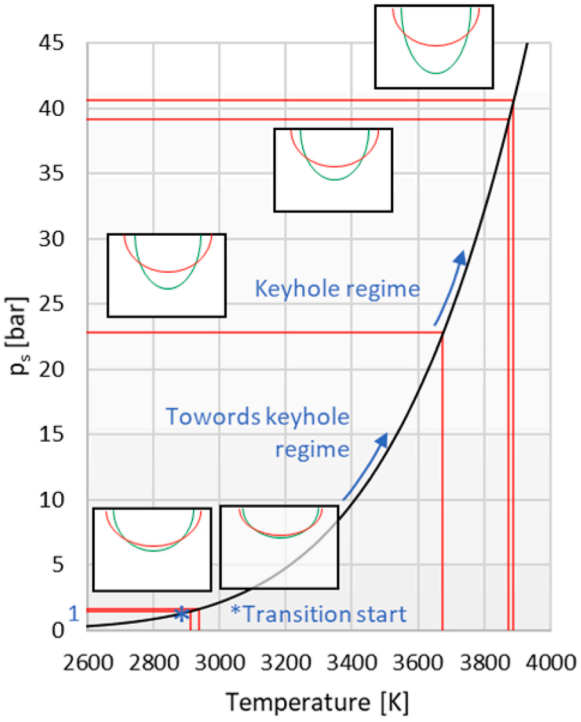

Fig. 14. Surface pressure at temperature variations calculated using Clasius-Clapeyron equation and p_s values calculated for the five cases of interest.

defects identified in the components following the interaction with the laser. Indeed, at lower fluence, the high thermal conductivity of copper allows a rapid heat transfer, preventing the large concentration of energy in the melted volume and limit the formation of pores due to metal vapor formation. However, the melted metal solidifies more quickly at the interface with the base material and if there was gas inside the melt pool it doesn't have the time to be expulsed from the weld, remaining trapped in the external part of the solidified metal. At fluence increasing the re-solidification velocity is lower while turbulence effects, Marangoni convection processes, buoyancy forces and surface boiling may

Table 6
Calculated maximum temperature and heating speed of divergence models.

	1500_5	1500_10	1350_5	1350_10	1200_5
Max Temperature [°C]	3889	3875	3676	2912	2939
Heating rate [°C/s]	6.19×10^4	2.76×10^4	2.72×10^4	4.48×10^4	2.28×10^4

disperse pores in different directions along the translation of the laser beam. Because of all of these factors, the presence of pores within the melted area is highly probable.

5. Conclusions

The effects of high-power blue laser source interaction in 2.3 mm thick commercial pure copper sheets were investigated to identify the conduction-to-keyhole regime transition. Experiment-based tests and simplified numerical simulation were used to identify the change of the interaction mode by evaluating the geometry of the laser-affected volume.

The comparison of experimental and numerical results revealed a very precise fitting of the data until the interaction regime is of complete conduction, allowing for the identification of a linear relationship between the absorption coefficient and the laser fluence. As soon as the laser-material interaction achieve the transition regime, analyzed data lose their convergence, and the error (in terms of molten volume) grows linearly with the increase in the energy density supplied to the system. The non-convergence of the data, because of the transition from conduction-to-keyhole regime, was verified starting from the analysis of three process conditions deemed necessary for the occurrence of the keyhole itself:

- Critical irradiance on the order of 0.5 MW/cm^2 is used for all test conditions.
- Divergence tests are characterized by melted and resolidified sections with aspect ratios greater than 0.5.
- Under the same process conditions of the preceding points, the boiling temperature has always been outdated.

Starting from these statements vapor surface pressure was calculated using Clasius-Clapeyron and a clear transition from conduction to keyhole mode was revealed when the calculated surface pressure reaches 22 bar. Based on these findings, it is possible to conclude that using current blue laser sources (BPP 30 mm/mrad and maximum power 1500 W), it is possible to identify process conditions in the keyhole regime during the interaction with pure copper if surface vapor pressure exceeds 22 bar and the energy density assumes value in the order of 7×10^4 J/cm^2.

CRediT authorship contribution statement

Erica Liverani: Conceptualization, Methodology, Writing – original draft. **Alessandro Ascari**: Investigation. **Luca Tomesani**: Supervision. **Alessandro Fortunato**: Validation, Writing – review & editing.

Declaration of Competing Interest

The authors declare that they have no known competing financial interests or personal relationships that could have appeared to influence the work reported in this paper.

Data Availability

Data will be made available on request.

References

Assaela, M.J., Kalyva, A.E., Antoniadis, K.D., 2010. Reference data for the density and viscosity of liquid copper and liquid tin. J. Phys. Chem. Ref. Data 39, 033105. https://doi.org/10.1063/1.3467496.

Baba, Y., Inoue, T., Sugioka, K., Kobatake, H., Fukuyama, H., Kubo, M., Tsukada, T., 2012. Thermal conductivity measurement of molten copper using an electromagnetic levitator superimposed with a static magnetic field. Meas. Sci. Technol. 23, 045103 https://doi.org/10.1088/0957-0233/23/4/045103.

Cunningham, R., Zhao, C., Parab, N., Kantzos, C., Pauza, J., Fezzaa, K., Sun, T., Rollett, A. D., 2019. Keyhole threshold and morphology in laser melting revealed by ultrahigh-speed x-ray imaging. Science 363 (6429), 849–852. https://doi.org/10.1126/science.aav4687.

Engler, S., Ramsayer, R., Poprawe, R., 2011. Process studies on laser welding of copper with brilliant green and infrared lasers. Phys. Procedia 12, 339–346. https://doi.org/10.1016/j.phpro.2011.03.142.

Franco, D., Oliveira, J.P., Santos, T.G., Miranda, R.M., 2021. Analysis of copper sheets welded by fiber laser with beam oscillation. Opt. Laser Technol. 133, 106563 https://doi.org/10.1016/j.optlastec.2020.106563.

Haubold, M.W., Zäh, M.F., 2019. Advantages of adjustable intensity profiles for laser beam welding of steel copper dissimilar joints. Procedia CIRP 79, 159–164. https://doi.org/10.1016/j.procir.2020.09.103.

Heider, A., Stritt, P., Hess, A., Weber, R., Graf, T., 2011. Process stabilization at welding copper by laser power modulation. Phys. Procedia 12, 81–87. https://doi.org/10.1016/j.phpro.2011.03.011.

Hess, A., Schuster, R., Heider, A., Weber, R., Graf, T., 2011. Continuous wave laser welding of copper with combined beams at wavelengths of 1030 nm and of 515 nm. Phys. Procedia 12, 88–94. https://doi.org/10.1016/j.phpro.2011.03.012.

Hügel, H., Dausinger, F., 2004. In: Laser Physics and Applications, Subvolume C: Laser Applications, VIII Vol. 1:. Springer, Berlin.

Kesharwani, R., Kumar Jha, K., Sarkar, C., Imam, M., 2022. Numerical and experimental analysis on friction stir welding of the dissimilar materials 6061-T6 AA and pure copper. Mater. Today.: Proc. 65, 3132–3142. https://doi.org/10.1016/j.matpr.2022.05.353.

Liebl, S., Wiedenmann, R., Ganser, A., Schmitz, P., Zaeh, M.F., 2014. Laser welding of copper using multi mode fiber lasers at near infrared wavelength. Phys. Procedia 56C, 591–600. https://doi.org/10.1016/j.phpro.2014.08.047.

Maina, M.R., Okamoto, Y., Okada, A., Närhi, M., Kangastupa, J., Vihinen, J., 2018. High surface quality welding of aluminum using adjustable ring-mode fiber laser. J. Mater. Process. Technol. 258, 180–188. https://doi.org/10.1016/j.jmatprotec.2018.03.030.

Mohammadpour, M., Wang, L., Kong, F., Kovacevic, R., 2020. Adjustable ring mode and single beam fiber lasers: a performance comparison. Manuf. Lett. 25, 50–55. https://doi.org/10.1016/j.mfglet.2020.07.003.

Nakamura, S., Sakurai, M., Kamimuki, K., Inoue, T., Ito, Y., 2000. Detection technique for transition between deep penetration mode and shallow penetration mode in CO_2 laser welding of metals. J. Phys. D: Appl. Phys. 33, 2941. https://doi.org/10.1088/0022-3727/33/22/311.

Ni, Z.L., Liu, Y., Wang, Y.H., He, B.Y., 2022. Interfacial bonding mechanism and fracture behavior in ultrasonic spot welding of copper sheets. Mater. Sci. Eng.: A 833, 142536. https://doi.org/10.1016/j.msea.2021.142536.

Ning, J., Zhang, L.J., Wang, A., Bai, Q.L., Yang, J.L., Zhang, J.X., 2016. Effects of double-pass welding and extrusion on properties of fiber laser welded 1.5-mm thick T2 copper joints. J. Mater. Process. Technol. 237, 75–87. https://doi.org/10.1016/j.jmatprotec.2016.06.011.

Ning, J., Zhang, L.J., Zhang, L.L., Long, J., Yin, X.Q., Zhang, J.X., Na, S.J., 2020. Effects of power modulation on behaviours of molten pool and keyhole during laser–arc hybrid welding of pure copper. Mater. Des. 194, 108829 https://doi.org/10.1016/j.matdes.2020.108829.

Punzel, E., Hugger, F., Dörringer, R., Dinkelbach, T.L., Bürger, A., 2020. Comparison of different system technologies for continuous-wave laser beam welding of copper. Procedia CIRP 94, 587–591. https://doi.org/10.1016/j.procir.2020.09.081.

Rinne, J.S., Nothdurft, S., Hermsdorf, J., Kaierle, S., Overmeyer, L., 2020. Advantages of adjustable intensity profiles for laser beam welding of steel copper dissimilar joints. Procedia CIRP 94, 661–665. https://doi.org/10.1016/j.procir.2020.09.103.

Rüttimann, C., Holtz, R., 2011. Reliable laser welding of highly reflective materials. Proceeding of SPIE, SPIE Eco-Photonics 2011: Sustainable Design, Manufacturing, and Engineering Workforce Education for a Green Future, Strasbourg, France, pp 80650X.

Stritt, S., Weber, R., Graf, T., Muller, S., Ebert, C., 2011. Utilizing laser power modulation to investigate the transition from heat-conduction to deep-penetration welding. Phys. Procedia 12, 224–231. https://doi.org/10.1016/j.phpro.2011.03.029.

Wu, D., Sun, J., Li, Z., Huang, J., Feng, K., 2023. Molten pool behaviors and energy absorption in coaxial hybrid blue-IR lasers welding of a copper material. Int. J. Therm. Sci. 184, 107945 https://doi.org/10.1016/j.ijthermalsci.2022.107945.